Tellus
SERIES B
CHEMICAL
AND PHYSICAL
METEOROLOGY
PUBLISHED BY THE INTERNATIONAL METEOROLOGICAL INSTITUTE IN STOCKHOLM

Tellus (2009), 61B, 216–228
Printed in Singapore. All rights reserved

TELLUS

Spectral aerosol optical depth characterization of desert dust during SAMUM 2006

By C. TOLEDANO[1]*, M. WIEGNER[1], M. GARHAMMER[1], M. SEEFELDNER[1], J. GASTEIGER[1], D. MÜLLER[2] and P. KOEPKE[1], [1]*Meteorological Institute, Ludwig–Maximilians–Universität,Theresienstr. 37, 80333 Munich, Germany;* [2]*Leibniz Institute for Tropospheric Research, Permoserstr. 15, 04318 Leipzig, Germany*

(Manuscript received 28 December 2007; in final form 1 August 2008)

ABSTRACT

The aerosol optical depth (AOD) in the range 340–1550 nm was monitored at Ouarzazate (Morocco) during the Saharan Mineral Dust Experiment (SAMUM) experiment in May–June 2006. Two different sun photometers were used for this purpose. The mean AOD at 500 nm was 0.28, with a maximum of 0.83, and the mean Ångström exponent (AE) was 0.35. The aerosol content over the site changed alternatively from very low turbidity, associated to Atlantic air masses, to moderate dust load, associated to air masses arriving in the site from Algeria, Tunisia and Libya. The dusty conditions were predominant in the measurement period (78% of data), with AOD (500 nm) above 0.15 and AE below 0.4. The spectral features of the AOD under dusty conditions are discussed. Air mass back trajectory analysis is carried out to investigate the origin and height patterns of the dust loaded air masses. The advection of dust occurred mainly at atmospheric heights below 3000 m, where east flow is the predominant. At the 5000 m level, the air masses originate mainly over the Atlantic Ocean. Finally the Optical Properties of Aerosols and Clouds (OPAC) model is used to perform a set of simulations with different aerosol mixtures to illustrate the measured AOD and AE values under varying dust concentrations, and a brief comparison with other measurement sites is presented.

1. Introduction

The influence of the mineral aerosol on climate is subject of intense study (Arimoto, 2001; Goudie and Middleton, 2001), due to the wide range and uncertainties in the radiative forcing produced by this type of particles (Sokolik et al., 2001; Myhre et al., 2003; Tanré et al., 2003). Specially relevant are the uncertainties related to the non-sphericity and the absorption by mineral particles (see Müller et al., 2008; Petzold et al., 2008; Wiegner et al., 2008, this issue and references therein).

In the Northern Hemisphere, the Saharan desert is the main source of mineral aerosol particles (Prospero et al., 2002). The Saharan dust affects the atmosphere composition and air quality over the Mediterranean countries and often western and central Europe (e.g. Bergametti et al., 1989; Guerzoni and Chester, 1996; Avila et al., 1997; Rodríguez et al., 2001; Ryall et al., 2002; Pace et al., 2006). A number of studies has been also carried out about the dust transport across the Atlantic to the Caribean Sea and southeastern U.S. (e.g. Prospero, 1999).

To reduce the uncertainties related to the mineral aerosol, many different types of measurements are accomplished: ground-based, satellite, aircraft, etc., with different approaches and temporal and spatial scales. Aerosol monitoring networks like AERONET (Holben et al., 1998) or GAW (Werhli, 2000) have established a number of measurement sites in North Africa and insular locations nearby (Canary Islands, Cape Verde). The spatial coverage of the satellite measurements makes possible the analysis of dust plumes optical properties and the transport events (Kaufman et al., 2001; Prospero et al., 2002; Chiapello et al., 2005; Kaufman et al., 2005). On the other hand, a major enhancement in the characterization of the Saharan dust was provided by characterization experiments like ACE-2 (Raes et al., 2000), SAFARI (Haywood et al., 2003a) or SHADE (Tanré et al., 2003; Haywood et al., 2003b).

The SAMUM experiment took place in Morocco during May–June 2006. The objective of this experiment was to carry out an intense investigation about the mineral dust close to the sources and also during transport events toward southwestern Europe: chemical, microphysical and optical properties. For this purpose, different types of instruments operated coordinately, both ground-based and airborne: sampling instrumentation, particle counters, lidars, sun photometers, etc. An overview of the campaign and all the work developed in the frame of SAMUM can be found in Heintzenberg (2008).

Remote sensing from ground-based sun photometry is a very effective method to investigate the aerosol optical properties.

*Corresponding author.
e-mail: carlos@meteo.physik.uni-muenchen.de
DOI: 10.1111/j.1600-0889.2008.00382.x

Sun and sky photometers allow a continuous monitoring of the atmospheric turbidity under cloud-free conditions. The aerosol optical depth (AOD) measured at different wavelengths of the solar spectrum is a key parameter in aerosol studies, together with the single scattering albedo and the asymmetry parameter (Dubovik et al., 2002). During the SAMUM experiment, several photometers operated in the measurement sites at Ouarzazate and Zagora. The interest of these data is based on three reasons: first, they provide effective temporal coverage of the atmospheric aerosol conditions. Second, the sun photometer data enhance the capability of the co-located instruments, for example, the Lidars, and provide 'ground-truth' for satellite retrievals validation. Third, a valuable set of data is obtained in conditions of pure Saharan dust aerosol.

The aim of this paper is to report the spectral AOD and its variability during the SAMUM experiment, with emphasis in the spectral features. Hence the direct sun measurements of the SSARA and Cimel photometers operating in Ouarzazate from 5 May to 12 June 2006 will be analysed. In Section 2, the site and instruments are described. The method is summarized in Section 3, and then the results are presented in Section 4, including the analysis of the AOD, back trajectories, simulations with the OPAC model and comparison with other sites. Finally, the conclusions are reported in Section 5.

2. Site of measurements and instrumentation

2.1. Site of measurements

The sun photometers were located in Ouarzazate airport (30.9°N, 6.9°W, elevation 1133 m a.s.l.), in Morocco. The site is located between the Atlas Mountains and the Anti-Atlas. The location is indicated in Fig. 1, as well as Zagora, the other location for AOD measurements during SAMUM (von Hoyningen-Huene et al., 2008, this issue). Ouarzazate is on a flat basin (100 × 50 km Approx.) with sparse vegetation and intense solar heating during the measurement period. In this region, easterly winds prevail in the lower troposphere up to 2500 m above ground level (a.g.l.) in May–June, as it will be shown by means of back trajectories in Section 4.2. The Ouarzazate village nearby (40 000 inhabitants) is located south of the airport, but no substantial local urban or industrial pollution is expected to be affecting the aerosol measurements. The weather conditions in the site were very appropriate for sun photometer measurements. There are data available for 38 out of 39 d of campaign, although some rainfalls occurred as well.

2.2. Instrumentation

The AOD data presented in this work were obtained with the Sun-Sky Automatic RAdiometer (SSARA, Wagner et al., 2003). It is mounted on a two-axis tracking system, which allows an accurate and fast pointing of the sensor head (Seefeldner et al., 2004). Both systems were developed by the Meteorological Institute of the University of Munich. The pointing is made alternatively by astronomical calculation or by a 4-quadrant detector. The tracking system switches automatically between these two modes, depending on the radiance with respect to a preset threshold. In case of astronomical calculation, the maximum pointing error is $<0.3^{\circ}$.

Fig. 1. Location of Ouarzazate and Zagora SAMUM-sites in Morocco, as well as several AERONET sites in the region.

The sun photometer is equipped with 15 separate and simultaneously measuring spectral channels, 12 for direct sun measurements and 3 almucantar channels, selected by means of interference filters. The channels in the range 340–1550 nm are summarized in Table 1. Each channel has its own collimator and detector. UV enhanced Si detectors are used in the spectral range 340–1030 nm and an InGaAs detector for 1550 nm. The electronic amplification is also adapted to the signal intensity in each channel. The field of view (FOV) for all channels is 1.2°. Unfortunately an amplification problem in the UV channels resulted in low signal-to-noise ratio, which must be taken into account in the data analysis.

The radiometer tracks the sun continuously except during the sky measurements in the solar almucantar, and the configuration of the system, with independent detectors and collimators, allows continuous monitoring of the AOD. Direct sun measurements are sampled every 2 s. Almucantar sky measurements are performed at fix solar zenith angles, each 5° at SZA $> 60^{\circ}$, in the morning and evening. The almucantar data are not included in this study.

The detectors inside the sensor head are stabilized in temperature to 40 °C, avoiding any problems derived from temperature dependence in the detection system. However, due to the intense

Table 1. Spectral channels of the SSARA sun photometer, exact central wavelengths (nm) and full width at half maximum (FWHM)

	λ (nm)	FWHM (nm)
Direct sun channels		
1	339	5
2	379	6
3	439	5
4	500	8
5	615	4
6	673	6
7	781	6
8	875	10
9	910	10
10	953	9
11	1031	6
12	1553	11
Almucantar channels		
13	439	5
14	781	5
15	1030	5

insolation in Ouarzazate around noon, the sensor head had to be cooled down in the hottest days. Besides, to avoid dust accumulation on the optical path, the front quartz window of the instrument had to be cleaned regularly during the campaign.

As a summary, the SSARA sun photometer provides 10 direct sun spectral channels in the range 340–1550 nm, suitable for aerosol research (plus two channels for water vapour determination). Therefore, it is an appropriate instrument for the investigation of spectral features in the AOD.

An AERONET-Cimel sun photometer was also deployed at Ouarzazate (Müller et al., 2008, pers. comm.). This instrument has extensively proved its capability for aerosol monitoring worldwide (Holben et al., 2001). See Holben et al. (1998) and the AERONET web page for a description of the instrument, data processing and calibration procedures.

3. Method

The direct sun measurements at ground level at each spectral channel $F(\lambda)$ allow the determination of the total optical depth of the atmosphere (τ). Using the Beer–Bouguer–Lambert law:

$$F(\lambda) = F_0(\lambda) \times \mathrm{e}^{(-\tau \cdot m)}, \quad (1)$$

where $F_0(\lambda)$ is the extraterrestrial signal of the instrument, corrected by the earth–sun distance and m is the airmass in the measurement path (Kasten and Young, 1989).

Aerosol optical depth (AOD or τ_a) is derived from the total optical depth, taking into account the Rayleigh optical thickness (τ_R) corrected by local pressure (P) and the gaseous absorptions (τ_g):

$$\tau_a = \tau - \tau_R \times P/P_0 - \tau_g. \quad (2)$$

The channels used for aerosol investigation are located in spectral regions with weak absorption due to atmospheric gases. Ozone absorption was taken into account in 340, 500, 615 and 674 nm. For this correction regular measurements of the total ozone column were performed with a Microtops photometer. The CO_2 absorption was taken into account in the 1550 nm channel. The absorption coefficients provided by Gueymard (1995) weighted with the filters transmission curves have been used to calculate the effective absorption coefficients in the different channels.

The AOD data at different wavelengths allow the determination of the Ångström exponent (AE; Ångström, 1961), according to

$$\tau_a(\lambda) = \beta \times (\lambda)^{-\alpha}. \quad (3)$$

To determine the AE, a linear fit of AOD versus wavelength in log–log scale is performed, giving, as result, a representative value for the spectral range considered. Four AOD channels of SSARA (440, 500, 675 and 870 nm) are used for this retrieval, so that the AE obtained is comparable with the AE provided by AERONET, also calculated in the spectral range 440–870 nm.

An automatic cloud-screening algorithm, based on temporal variability of the measured AOD, is applied to remove cloud contamination in the data. For this purpose, minutes with AOD (870 nm) dispersion larger than 0.01 were labelled as 'cloudy'. After this filtering, which is easily tunable, a manual inspection was also carried out to remove some remaining bad data in case of stable thin clouds. The sampling rate of 2 s is an advantage for cloud detection, and no other temporal derivatives of the AOD, like those applied in AERONET cloud-screening algorithm (Smimov et al., 2000), needed to be analysed to make the cloud screening. According to the cloud-coverage observations during the campaign and comparing the AOD before and after cloud-screening, the filtering did not remove valid AOD data under dusty conditions but some weak cloud contamination by cirrus could remain.

The extraterrestrial signal $F_0(\lambda)$ is taken as the calibration coefficient for each spectral channel. This calibration was obtained by the Langley plot method in the Environmental Research Station Schneefernerhaus (2650 m a.s.l., in the Zugspitze mountain, Germany), both before and after the SAMUM campaign. This high altitude station provides very good conditions for absolute calibration of sun photometers, especially in spring. The absolute errors in the retrieved AOD, taking into account uncertainties in the calibration, gases and Rayleigh corrections and dirtiness in the front window, are less than 0.025 for all channels except those in the UV, which due to the amplification problem have larger uncertainty (absolute error <0.05). Note that systematic AOD errors due to calibration are modulated by the airmass, thus smaller in the morning and evening and larger around noon.

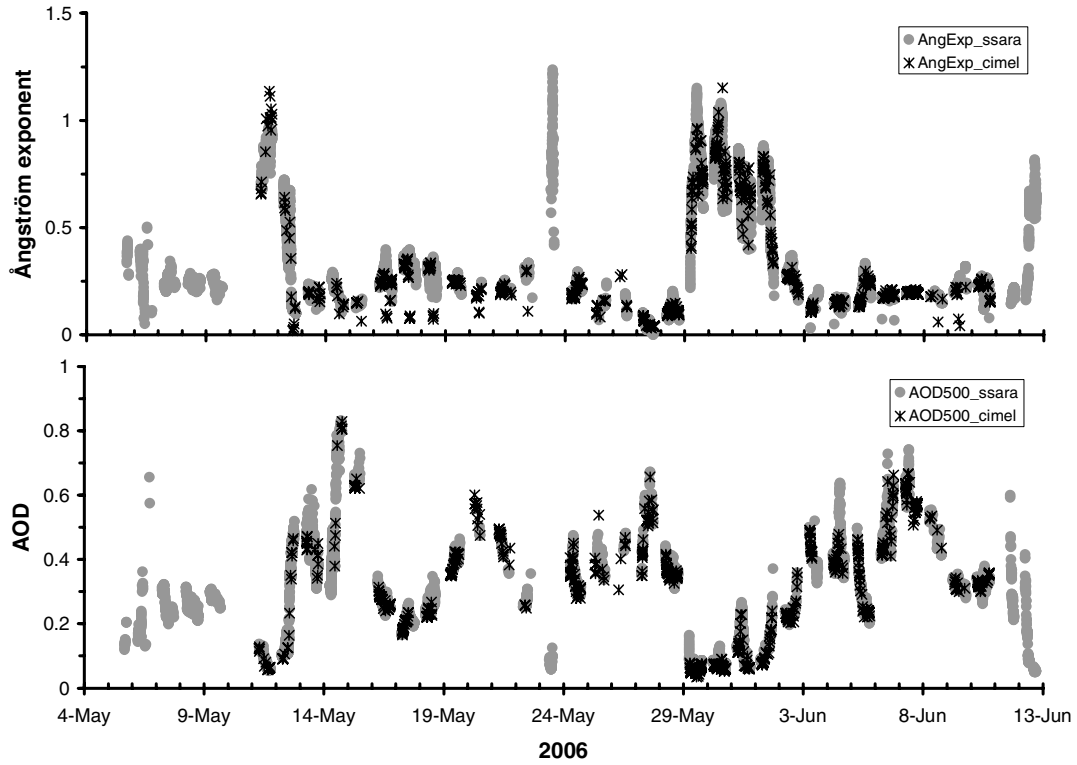

Fig. 2. Time-series of aerosol optical depth at 500 nm (lower panel) and Ångström exponent (upper panel) in Ouarzazate, obtained with the SSARA sun photometer and the AERONET-Cimel. SSARA data are cloud-free minute averages. Cimel data are AERONET level 2.0 data.

4. Results

4.1. AOD and Ångström exponent

The AOD during the campaign allows a detailed monitoring of the dust in the atmosphere above Ouarzazate. The analysis of this parameter will be illustrated with the help of back trajectories and the OPAC model. It is well known from literature that the extinction by desert dust exhibits low spectral dependence frequently represented by low AEs. The variability in the AOD is large, with typical AOD (500 nm) of 0.3–0.5 and peaks up to 2.5 or more during severe dust storms (Tanré et al., 1988; Holben et al., 2001; Dubovik et al., 2002).

In this section, we want to describe the AOD measurements performed with the SSARA photometer. The conditions encountered in the site mainly correspond to pure dust, with varying intensity along the campaign. However, several days registered very low turbidity, which is very helpful to establish a background aerosol for this area.

The AOD and AE time-series for the SAMUM experiment are displayed in Fig. 2. In this plot, both the SSARA and AERONET-Cimel data (Müller et al., 2008, pers. comm.) are shown. The coverage of the SSARA data is larger, both in sampling time and measurement period (5 May to 12 June). In this figure, cloud-free minute averages of SSARA AOD and AE are included. The agreement between the instruments in both parameters is satisfactory, with absolute AOD differences below 0.03 in the range 340–440 nm and below 0.02 in 500–1550 nm wavelengths, thus within the reported experimental errors. The absolute differences in the AE are also within the typical errors (better than 0.05 for AOD (440 nm), >0.15, and better than 0.1 for AOD (440 nm), <0.15.

A statistical summary of the spectral AOD and the AE is given in Table 2. The mean AOD (500 nm) for the entire measurement period was 0.28 (with standard deviation $SD = 0.15$), but it ranged from 0.05 to 0.83, that is, from almost pristine conditions to severe dust load in the atmosphere. The AOD shows in general low spectral dependence, with mean AE of 0.35. Although not included in this work, the statistics for the water vapour content (in cm) are also reported in this table.

Successive episodes of turbid and clean atmosphere occurred during the campaign. When the dust is present, the AOD ranges from 0.2 to 0.8, approximately, and the AE is below 0.4. For quasi dust-free conditions, we find AOD below 0.1 and AE above 0.6, approximately. These two scenarios can be clearly identified in the frequency histograms of the AOD and AE, which are presented in Fig. 3. In both parameters, two distinct frequency modes are found in the measurements. In the AOD (500 nm), Fig. 3(a), the first mode centred in 0.06 correspond to the background conditions, approximately 22% of the data. The corresponding measurements of the AE (Fig. 3b) constitute

Table 2. Mean, standard deviation (*SD*), maximum, minimum and median values for the spectral AOD (nominal wavelengths), Ångström exponent (AE) for two spectral ranges and water vapour content obtained in Ouarzazate with the SSARA sun photometer

(nm)	Mean	*SD*	Max	Min	Median
AOD (340)	0.294	0.146	0.847	0.043	0.287
AOD (380)	0.293	0.147	0.847	0.060	0.279
AOD (440)	0.291	0.147	0.840	0.062	0.281
AOD (500)	0.277	0.147	0.831	0.050	0.264
AOD (615)	0.256	0.147	0.808	0.035	0.242
AOD (675)	0.260	0.146	0.808	0.040	0.247
AOD (780)	0.259	0.145	0.785	0.041	0.248
AOD (870)	0.245	0.142	0.760	0.030	0.234
AOD (1030)	0.235	0.128	0.678	0.025	0.233
AOD (1550)	0.203	0.116	0.622	0.021	0.195
AE(440–870)	0.353	0.244	1.236	−0.012	0.256
AE(340–500)	0.280	0.261	1.240	−0.023	0.223
Water (cm)	0.902	0.293	1.809	0.250	0.868

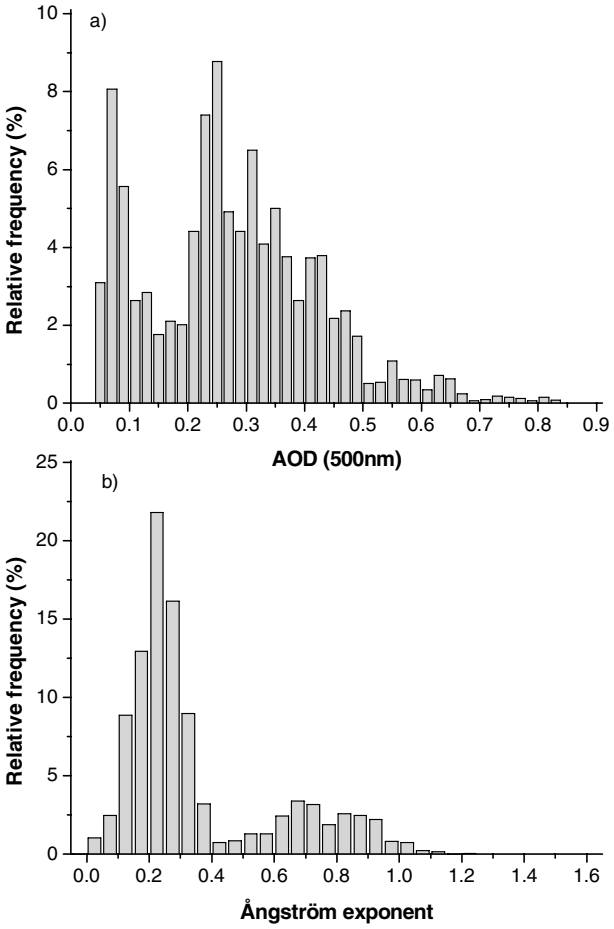

Fig. 3. Frequency histograms of the AOD (500 nm) and Ångström exponent in Ouarzazate.

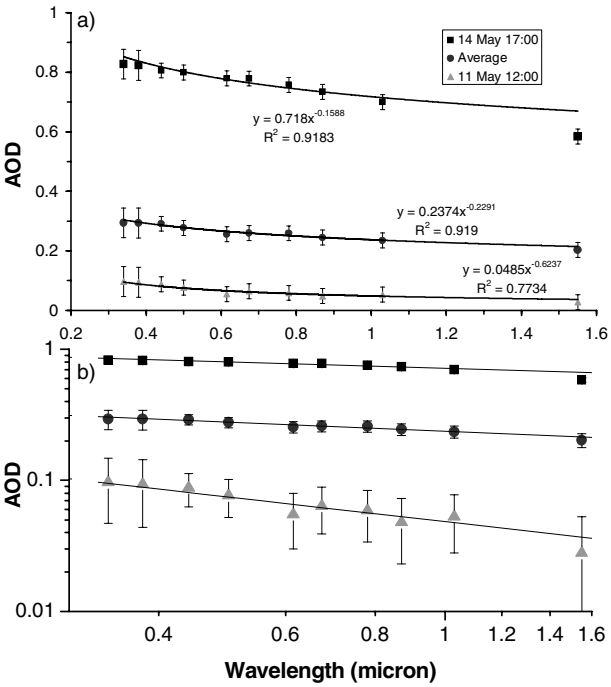

Fig. 4. (a) Wavelength dependence of the aerosol optical depth for average conditions (circles), severe dust (squares) and background conditions (triangles); (b) Same in log–log scale.

a mode centred in 0.7, which includes 24% of the observations. The AOD larger than 0.15 (78% of the data) are related to the main mode in the AE, centred in 0.2, which is a clear signature of desert dust.

The AOD wavelength dependence is illustrated in Fig. 4(a). The average AOD spectrum is shown in the middle of the plot, whereas the upper part corresponds to the maximum AOD observed on 14 May and the lower part to a clean case (30 May). The fit to the Ångström power law is also depicted. The departure from the fit curve is in all cases less than the experimental errors (indicated by error bars) except in 1550 nm, as can be seen in the upper example curve. Actually, it is a pattern in the data series that the departure of the AOD (1550 nm) from the Ångström fit increases for larger AOD. However, the differences AOD (measured) − AOD (Ångström fit) at this wavelength are only significant, that is, above the ±0.02 uncertinty for AOD(1550 nm)>0.4, reaching a maximum difference of 0.11 for a measured AOD (1550 nm) of 0.62 (Fig. 4a).

Therefore, we can consider that the power law is a good approximation for the desert dust aerosol up to 1030 nm. This is in agreement with the spectral AOD dependence, investigated by Eck et al. (1999) in the range 340–1020 nm, where important departures from the Ångström law (curvature) of the spectral AOD are observed in case of biomass burning aerosol but not in case of desert dust. In Fig. 4(b), the same AOD spectrum is presented in log–log scale, in which the Ångström fit is a straight line. Although the power law is a good fit in the spectral

Table 3. Summary of periods within the campaign (see text). For each period an insight about the dust conditions, the mean and extreme AOD (500 nm) and AE and some remarks are provided

Nr.	Dates	Dust	Mean AOD	Mean AE	Max AOD	Min AE	Remarks
1	5–9 May	low	0.25	0.27	0.66	0.06	Gusty wind in the afternoons. Cirrus and convective clouds.
2	10–11 May	no	0.08	0.88	0.14	0.68	Clouds and light rain on the 10th (no data this day).
3	12–15 May	high	0.38	0.28	0.83	0.10	Bright milky sky, light rain on 15th afternoon.
4	16–22 May	moderate	0.29	0.30	0.50	0.17	Weak easterly wind in the mornings. Convection and gusty wind in the afternoons. Light rain on 20th.
5	23 May	no	0.08	0.90	0.13	0.43	Wind from north-northwest. Dust devils after noon.
6	24–28 May	moderate	0.39	0.15	0.67	−0.01	Partly cloudy. Wind from east. Heavy rain and thunderstorm on the 26th.
7	29–31 May	no	0.09	0.78	0.27	0.23	Wind changing from east to north.
8	1–5 June	moderate	0.28	0.32	0.64	0.04	Convection in the afternoon hours. Light rain on 3rd.
9	6–12 June	high	0.35	0.26	0.74	0.07	Milky sky. Low wind mainly from south.

range 340–1030 nm, a certain curvature can be observed in the UV too. As we move towards shorter wavelenths, the increase in the measured AOD is less than the increase of the Ångström fit. This is consistent with the AE observed in the range 340–500 nm, which is lower than the 'standard' value calculated in the 440–870 nm spectral range (see Table 2).

However, we must be very cautious with these findings due to the large errors of the UV channels of the SSARA photometer during this campaign. The agreement in this point with the Cimel is not enough either, since the Cimel-340 nm channel did not rise the quality assured level 2.0 of AERONET. Therefore, the AOD spectral dependence of desert dust in the UV region will require further investigation, and special attention will be given to this topic during the next SAMUM campaign in January 2008.

According to the time-series in Fig. 2, we have distinguished several periods in the analysis. The periods have been established according to the day-to-day changes observed in the AOD. Thus, nine periods are found, with clear changes from dusty to clean conditions on days 12, 23 and 28 May. These changes are related to changes in the air masses, as it will be shown in Section 4.2. The dates of the periods and AOD–AE averages are described in Table 3.

At the beginning of the campaign (5–9 May, period 1), the AOD (500 nm) shows intermediate values, between 0.15 and 0.3 and AE between 0.15 and 0.40. Therefore, only moderate amount of dust was present, slightly increasing during the period. On 10 May, there are no measurements due to clouds, but on 11 May (period 2) the atmosphere is much cleaner, with AOD going down to background values (0.06) and the AE increasing correspondingly to 0.96. On 12 May, new dust arrives, with severe increase in the AOD during that day and the typical decrease of the AE. During the next days (12–15 May, period 3), the desert dust predominates, with a mean AOD of 0.38 (max 0.83 on 14 May) and AE below 0.25, in general. The AOD decrease on 16 May indicates some change in the conditions (16–22 May, period 4). There is also an increase in the AE, indicative of a smaller particle size, but in this case, the dust remains over the site until a new dust advection produces an increase in the AOD on 19 May.

On 23 May (period 5), the atmosphere was suddenly clean and the background AOD was observed, but only 1 d after the dust predominates again (24–28 May, period 6). In this period, the smallest values of the AE were measured, including some slightly negative values on day 27 May. The new clean event (29–31 May, period 7) was interrupted with some dust (maybe air mass recirculation) for some hours on 31 May. On 1 June, the AOD increase is indicative of dust arrival. The dust will remain until 12 June. However, due to the AOD change between 5 and 6 June, we can consider a first part of the episode (1–5 June, period 8) and a final period (6–12 May, period 9), with AOD and AE returning to background values on 12 June.

The AOD–AE scatter plot for the SSARA data is presented in Fig. 5. When several years of data are available, such a plot is an excellent description of the climatology of the aerosol properties (Eck et al., 1999; Holben et al., 2001; Toledano et al., 2007). For a limited data series, it is a valuable tool to find aerosol types and differences involving size predominance and amount of aerosol particles. The signature of desert dust, high turbidity due to large particles (low wavelength dependence), corresponds to the lower region of the AOD–AE scatter plot, just where we find the data from Ouarzazate. The nine different periods explained above (see Table 3) are displayed in different colours. Note the higher AE in period 4 (16–22 May) and the lowest AE values of period 6 (24–28 May), although the corresponding AOD is not the maximum observed. The rest of dust periods are very close together in the scatter plot. On the other hand, the data during

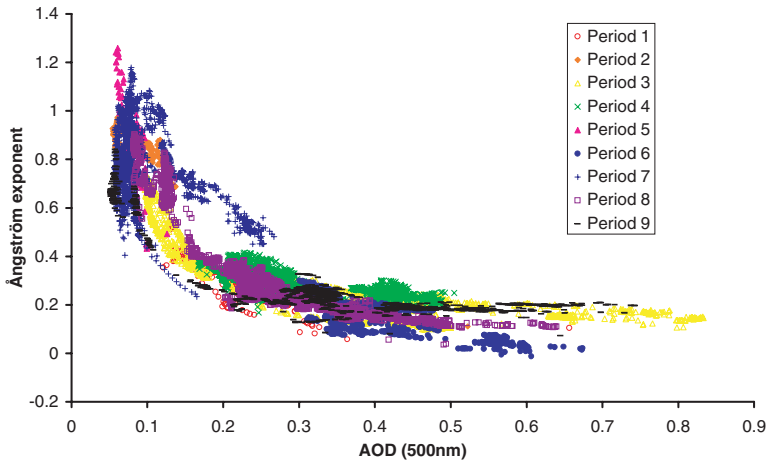

Fig. 5. Scatter plot of the AOD (500 nm) vs. Ångström exponent for the entire SSARA data set. The coluors correspond to the nine different periods within the time-series (see text and Table 3).

the clean periods (2, 5 and 7) are located in the upper-left-hand corner of the scatter plot, corresponding to lowest turbidity and relative predominance of smaller particles.

In the Lidar profiles (BERTHA and MULIS lidar systems, see Freudenthaler et al., 2008, this issue) some cirrus clouds are frequently observed on top of the dust layer, usually between 3 and 5 km height above ground. This cloud contamination could be responsible for the negative AE observed on 27 May. On this day, the Lidar measurements in the morning do not show clouds, but the evening measurement (after sunset) indicates the presence of thin clouds at 3 km height. Neither the AERONET-Cimel nor SSARA cloud-screening algorithms rejected the data, but it is unclear if they were contaminated by clouds.

4.2. *Back-trajectory analysis*

Back trajectories are a common tool used to determine the air mass origin (Stohl, 1998). Back trajectories for Ouarzazate have been calculated with the HYSPLIT model (Draxler and Rolph, 2003), using the FNL meteorological database and the model vertical velocity. For the entire measurement period, 5 d back trajectories for every day at 12 UTC at 4 atmospheric levels (500, 1500, 3000 and 5000 m a.g.l.) are calculated. In Fig. 6, these trajectories are shown for 500 and 3000 m a.g.l., with different plots for each of the nine periods established by the AOD analysis above (see Table 3). The aim of this section is to investigate whether the changes in AOD are linked to the air mass origin and describe the data that are related to each air mass origin.

In general, the predominant direction of the air flow is East at levels below 3000 m. In all cases except the period 4 (16–22 May), the air mass at 5000 m a.g.l. had Atlantic (westerly) origin. The clean periods (2, 5 and 7, Table 3) are characterized by the arrival of Atlantic air masses, in which the back trajectories show the air mass arrival from the west in all the atmospheric levels, except for 500 m in two (out of six) cases. A cyclonic turn (counterclockwise) is also observed for most of the Atlantic trajectories. Thus, the data indicate low turbidity only when a marine air mass comes over the site. This can also be an explanation for the AE (around 1) in the background cases, which is closer to the typical coastal AE rather than continental background (Hess et al., 1998; Smirnov et al., 2002).

Back trajectories have been calculated at 12 UTC, so, the changes of air mass might not be exactly reflected if it happened in the evening or night. However, Fig. 6 indicates that in general, every change in the aerosol was produced by air mass changes at a certain atmospheric level. Sometimes the change is sharp (from east to west origin) and involves all heights (e.g. 22–23 May). In other cases, the change is more gradual or only affects some of the investigated atmospheric levels (e.g. 15–16 May, with change only above 1500 m).

During the dusty periods, air masses from the East predominate in many cases with anticyclonic turn. The dust-loaded air masses originate in Algeria, Libya and Tunisia, especially for the 500 and 1500m heights. A typical example can be found on 4 June, Fig. 7(a): the 5000 m back trajectory comes from the Atlantic but for the heights below 3000 m the origin is north Algeria, arriving in Ouarzazate from the East. It is also interesting to see the vertical profile along the trajectories (bottom panel). On the left-hand side, it is the arrival point (Ouarzazate) at the mentioned heights above ground level. To the right-hand side, the height is plotted backwards in time for 5 d. The 5000 m trajectory (Atlantic) did not experiment relevant changes in height. But it can be clearly seen how the air mass below, after long residence time at ground level, was lifted as it travelled to the west towards the measurement site. Furthermore, the source region for 500 and 1500–3000 m is different, which resulted in different dust layers (Weinzierl et al., 2008, this issue). In Fig. 7(b), another example is shown—21 May. In this case, even the 5000 m level had its origin over Algeria, now arriving at the site from the south, with anticyclonic turn. Also interesting is the height profile, which indicates severe convection and the enlargement of the dust layer up to 5 km. The colocated Lidar measurements also confirm this point.

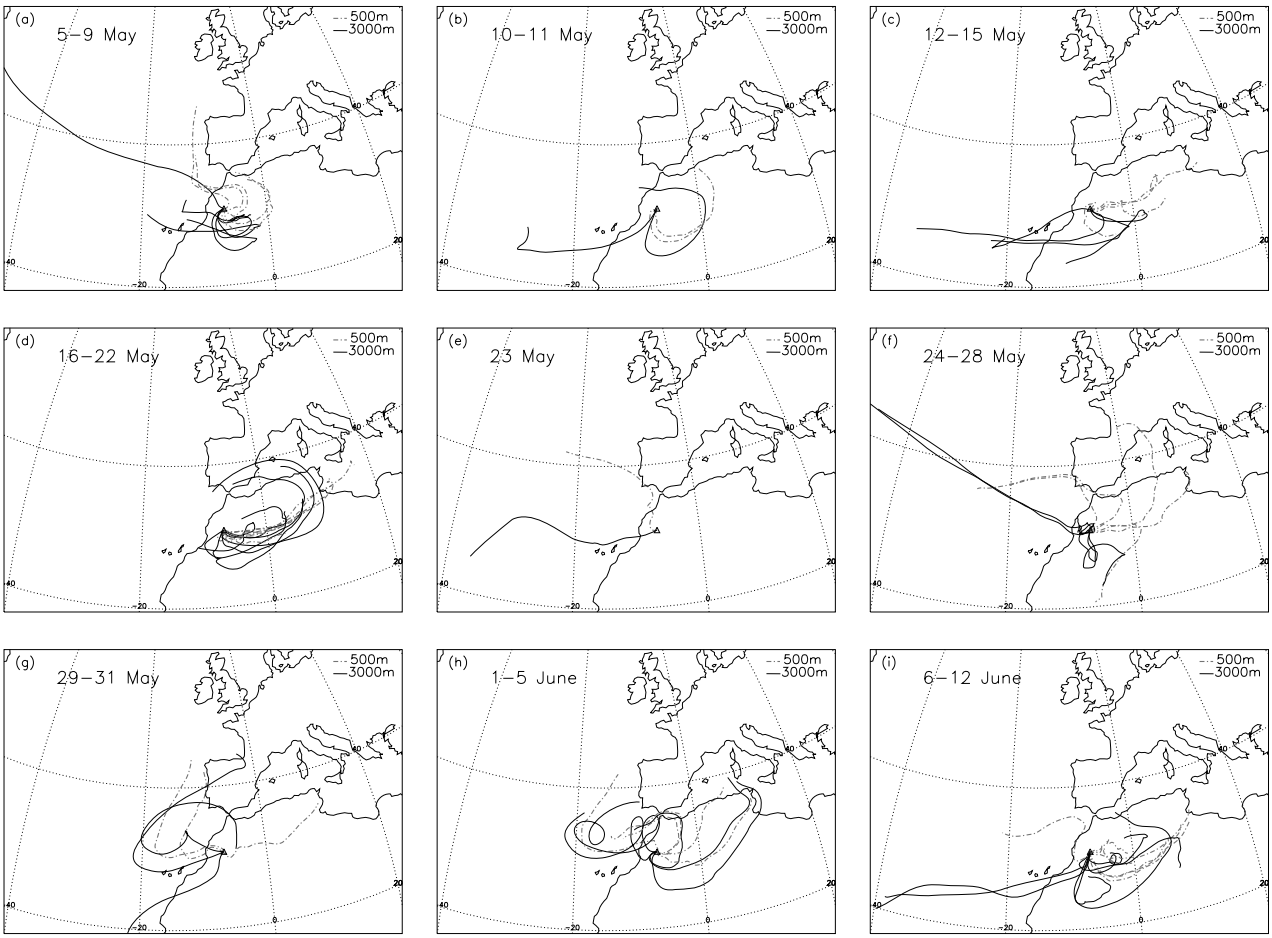

Fig. 6. 5-d back trajectories over Ouarzazate at 500 (grey dotted lines) and 3000 m (black lines) a.g.l. for each of the periods indicated in Table 3.

The back-trajectory analysis, together with the AOD-AE plot (Fig. 5) for the dusty periods, does not reveal great differences in the optical properties among the different source regions of dust. The low AOD (around 0.2–0.3) in case of air masses from Morocco and west Algeria (period 1 and 8 in Table 3 and Figs 6a and h) is notable. The dust load is larger for the air masses arriving from northeastern Algeria, Tunisia and the north of Libya. The associated AE does not indicate relevant changes in the particle size predominance for the different source regions.

4.3. Analysis with the OPAC model

In Fig. 5, the AOD–AE data close to the background values in periods 3 and 9 correspond to the arrival of dust (12 May) or the end of the dust event (12 June). As the amount of dust increases in the atmosphere, the AOD increases and the AE decreases. The opposite is observed at the end of dust periods. The OPAC model (Hess et al., 1998) can be used to calculate the optical properties of custom-defined mixtures of 10 aerosol components and thus has been used to describe the observations.

For the purpose of modelling the desert aerosols, a mixture of four components is considered, as proposed in the OPAC description. These are the water-soluble component (WASO) and three mineral components of different size, the mineral nucleation mode (MINM), mineral accumulation mode (MIAM) and mineral coarse mode (MICM). To represent the variability of desert aerosol, 18 simulations are performed, with a fixed number of water soluble but variable amount of mineral particles. WASO is taken into account with 500 or 2000 part cm^{-3} and three different values of relative humidity (RH = 0%, 50% and 80%). The amount of mineral particles is varied by its total number between 20 and 1000 part cm^{-3}, that is, between background conditions and dust storm.

With increasing total amount of particles, the relative amount of large particles also increases (Mélice et al., 1984; D'Almeida, 1987; Tanré et al., 2003; Kandler et al., 2008, this issue). Thus, the mixture of the three mineral components to describe the desert-dust size distribution is related to the turbidity, that is, to the total amount of mineral particles N_{mineral}, using the correlation given by Koepke et al. (1997):

$$\ln(N_{\mathrm{MINM}}) = 0.104 + 0.963 \times \ln(N_{\mathrm{mineral}}), \quad (4)$$

$$\ln(N_{\mathrm{MIAM}}) = -3.94 + 1.29 \times \ln(N_{\mathrm{mineral}}), \quad (5)$$

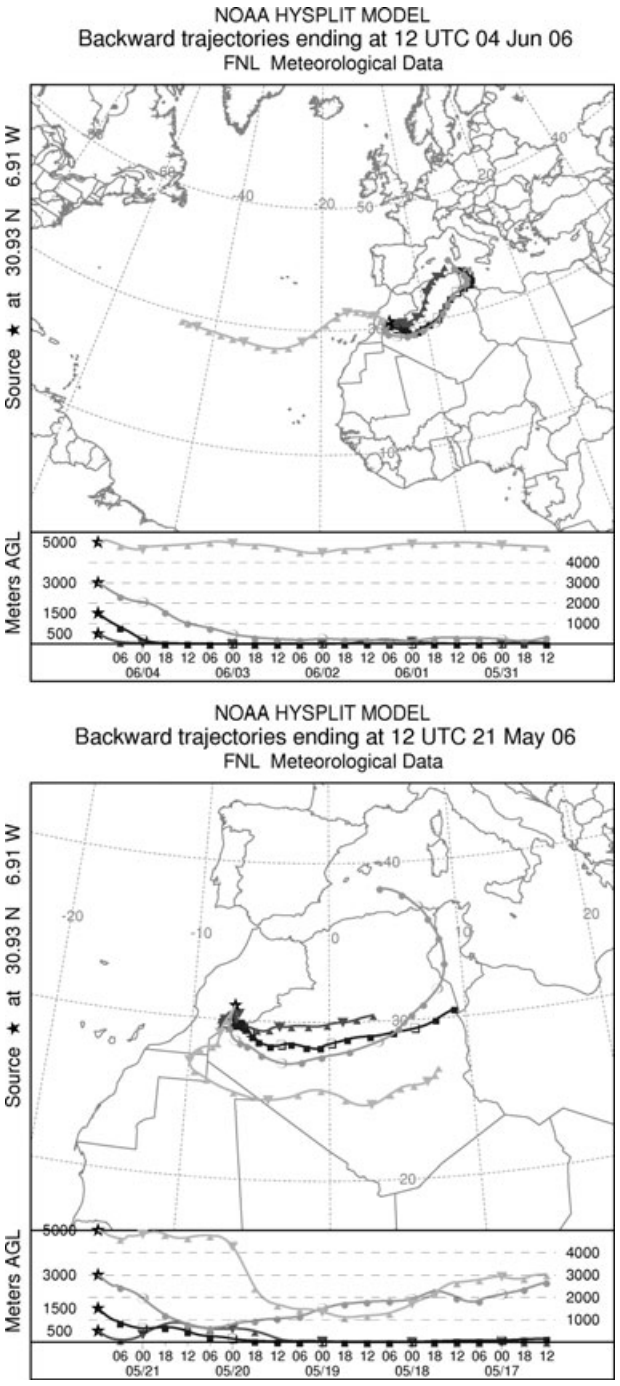

Fig. 7. Back trajectories over Ouarzazate on (a) 4 June and (b) 21 May.

$$\ln(N_{\mathrm{MICM}}) = -13.7 + 2.06 \times \ln(N_{\mathrm{mineral}}). \quad (6)$$

In Table 4 can be found the summary of the input parameters for these OPAC simulations, as well as the AOD and AE in the range 500–800 nm, modelled for each mixture and relative humidity. To calculate the AODs, an aerosol layer of 4 km height above ground and constant extinction coefficient has been assumed. Changes in the dust layer such as depth, height or height-dependent aerosol concentration are not considered in the simulations, but this is not relevant for the analysis that is intended here.

Obviously the optical depth increases as the mineral particle number increases. A gradual decrease in the AE is also observed, even reaching slightly negative values for the largest AODs. Furthermore, the result follows very faithfully the pattern observed in the SAMUM data, as we show in Fig. 8. In this plot, the OPAC simulations are displayed in the AOD-AE scatter plot, together with the real data. Almost all the measurements are within the range of the simulated cases; thus, the combination of water-soluble aerosol plus mineral aerosol is able to explain the observations, especially the evolution of the AE when the amount of dust changes. The AOD dependence on the RH comes only from the WASO component, and it is less relevant as the dust particle number increases.

If the WASO component is removed from the the mixture, it is not possible to describe the data, especially the AE values close to 1 for low turbidity. The WASO produces the AOD increase in the UV and the high AEs, when it is predominant. When the amount of dust increases, the WASO becomes less relevant and the AOD wavelength dependence disappears. For the most extreme dust cases (i.e. dust storm, see AOD up to 2.5 in Fig. 8), the AOD increases with wavelength. This effect was observed in the data as well (see Fig. 5). On the other hand, the AE for the UV, AE (350–500 nm), in the simulations (not shown) has very similar values to AE (500–800 nm) thus not indicating an AOD spectrum curvature as it was observed in the data (see Fig. 4).

4.4. Comparison with other sites

In Zagora site, another Cimel sun photometer operated as part of the SAMUM experiment. At the same time, a number of AERONET sites obtained data in the Saharan region and surroundings. The AOD properties in these sites have been analysed and compared with the observations in Ouarzazate.

Zagora is located 120 km southeast of Ouarzazate, south of the Anti Atlas mountain range, in the border of the Saharan desert. The AOD in Zagora is, in general, higher than at Ouarzazate, with mean AOD (500 nm) of 0.53 (von Hoyningen-Huene et al., 2008, this issue), but it must be noted that the elevation of Ouarzazate (1133 m) is higher than at Zagora site (680 m). The time-series for both sites (not shown) have similar evolution except for the period 22–27 May, in which the AOD at Zagora was much higher and variable. The mean AE was 0.24, very close to the observed values in Ouarzazate during the dusty periods (Table 3).

Three AERONET sites in the Saharan region have been considered: Agoufou (15°N, 1°W), in Mali; Tamanrasset (23°N, 6°E), in Algeria and Ras El Ain (32°N, 8°W), in Morocco (see Fig. 1). The AOD time-series are not considered here in detail since the various locations are separated by large distances.

Table 4. Summary of simulations with OPAC. Input parameters: particle number (cm^{-3}) for the water-soluble component (WASO), mineral nucleation mode (MINM), mineral accumulation mode (MIAM), mineral coarse mode (MICM) and mineral total. Output: AOD (500 nm) and Ångström exponent AE (500–800 nm) for three different relative humidities (RH)

	WASO	MINM	MIAM	MICM	MI total	RH = 0%		RH = 50%		RH = 80%	
	Particle Number (cm^{-3})					AE(500-800)	AOD500	AE(500-800)	AOD500	AE(500-800)	AOD500
1	500	19.11	0.89	0.001	20	0.58	0.03	0.71	0.04	0.82	0.05
2	2000	19.11	0.89	0.001	20	1.05	0.07	1.17	0.09	1.23	0.13
3	500	47.03	2.96	0.004	50	0.28	0.08	0.36	0.08	0.44	0.09
4	2000	47.03	2.96	0.004	50	0.61	0.11	0.76	0.14	0.88	0.17
5	500	92.66	7.32	0.015	100	0.14	0.16	0.18	0.17	0.23	0.18
6	2000	92.66	7.32	0.015	100	0.33	0.20	0.45	0.22	0.55	0.26
7	500	181.91	18.03	0.063	200	0.06	0.37	0.08	0.38	0.10	0.39
8	2000	181.91	18.03	0.063	200	0.15	0.41	0.21	0.43	0.28	0.47
9	500	269.37	30.48	0.14	300	0.02	0.62	0.03	0.63	0.05	0.64
10	2000	269.37	30.48	0.14	300	0.08	0.66	0.12	0.68	0.17	0.72
11	500	355.53	44.20	0.26	400	0.00	0.91	0.01	0.91	0.02	0.92
12	2000	355.53	44.20	0.26	400	0.04	0.94	0.07	0.97	0.11	1.00
13	500	440.65	58.93	0.41	500	−0.01	1.22	0.00	1.22	0.00	1.23
14	2000	440.65	58.93	0.41	500	0.02	1.25	0.04	1.28	0.07	1.31
15	500	608.34	90.83	0.83	700	−0.03	1.92	−0.02	1.93	−0.02	1.93
16	2000	608.34	90.83	0.83	700	−0.01	1.95	0.01	1.98	0.02	2.01
17	500	854.86	143.42	1.73	1000	−0.04	3.15	−0.04	3.16	−0.04	3.17
18	2000	854.86	143.42	1.73	1000	−0.03	3.18	−0.02	3.21	−0.01	3.25

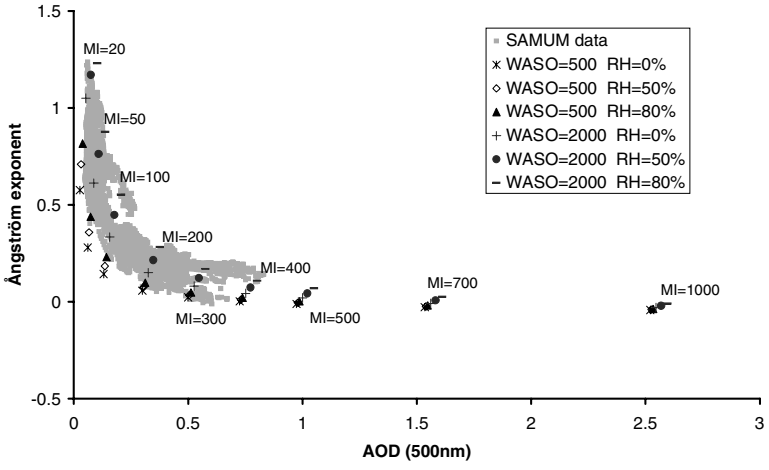

Fig. 8. Scatter plot of the AOD (500 nm) vs. Ångström exponent for the OPAC simulations (different black symbols) and the SSARA measurements during SAMUM (grey dots).

However, clear similarities in the time-series are found between Ouarzazate and Ras El Ain.

We are interested in the comparison of the aerosol type, evaluated in terms of AOD and AE, as it was described in the above sections. The scatter plots in Fig. 9 indicate that the same aerosol type is observed in Ouarzazate, Agoufou, Tamanrasset and Zagora (Figs 9a–c), although Agoufou presents much higher AOD, with an average of 0.64 at 440 nm. Looking at the site locations, we can assume that this is the signature of the pure dust on the AOD–AE plot. The elevation of Ouarzazate can also explain its lower background AOD. The mean AE in the period May–June 2006 was 0.14 in Agoufou and 0.19 in Tamanrasset, therefore close to, although smaller than, that at Ouarzazate. According to the OPAC simulations, this difference can be attributed to the larger aerosol load, which also implies an increased amount of large particles. Second, the larger AEs in the site Ras El Ain (Fig. 9d), with mean AE of 0.58, indicate a different aerosol type, probably a mixture of dust and other components, with an apportioning of fine particles. The mean AOD(440 nm) was 0.37. Ras El Ain is separated of Ouarzazate by the high Atlas mountains.

On the other hand, the AERONET sites Evora (38°N 8°W, Portugal) and Lampedusa (35°N, 16°E, Italy) have been analysed. Several events of dust transport toward Europe occurred

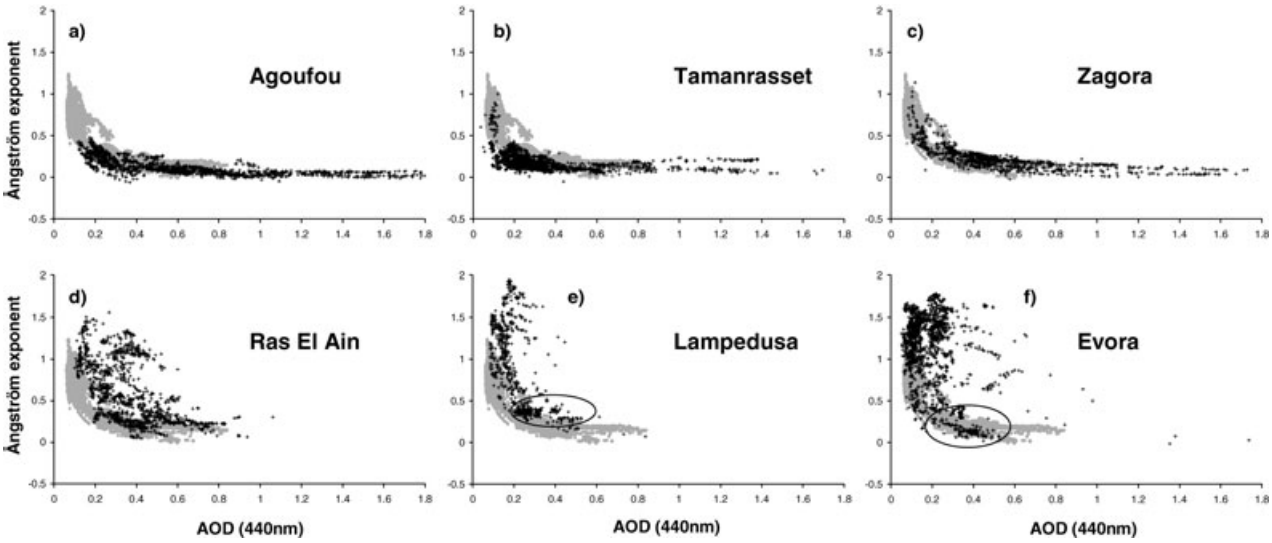

Fig. 9. Scatter plot of the AOD (440 nm) vs. Ångström exponent for various sites in the Saharan region and surroundings (in black) and the SSARA measurements in Ouarzazate (grey dots in all panels). In this case, the 440 nm channel is used since not all AERONET sites have a 500 nm channel. The circles in figures (e) and (f) indicate dust events.

during May and June 2006. The dust fingerprint over the AOD–AE plots has been investigated in these sites too. In Evora, where the mean AE for May–June was 1.10, there was a dust outbreak on 26–29 May (Wagner et al., 2008, this issue). This period shows a clear dust type (see Fig. 9f), with mean AOD (440 nm) of 0.37 and mean AE of 0.20, in agreement with the observations in the Saharan sites. However, the dust events in Lampedusa (9–13 May and especially 19–31 May) show, in general, AE values above 0.25, with a mean AE of 0.39 (Fig. 9e), larger than at the pure Saharan sites. The AOD was also moderate, with mean of 0.30 at 440 nm. This could indicate some reduction in the mean particle size along the transport, due to the deposition of the largest particles. The SAMUM-2 experiment, in Cape Verde islands, will investigate in detail the properties of the transported Saharan dust.

5. Conclusions

The AOD over Ouarzazate during the SAMUM experiment has been analysed. Successive episodes of moderate dust occurred within the measurement period. These episodes are separated by some few days in which the atmospheric turbidity was significantly low. This short clean periods are characterized by the arrival of Atlantic air masses over the site. The dust was linked to air masses arriving in Ouarzazate from the east and southeast, which were predominant wind directions at atmospheric levels below 3000 m. Above this level, the dominant wind direction is West. However, there were days with easterly flow up to 5000 m a.g.l., as it was confirmed by the dust layer height measured with lidar.

The mean AOD (0.28 at 500 nm wavelength) and AE (0.35) correspond to the typical values reported in the literature for desert dust. The AOD spectral dependence in the range 440–1030 nm is appropriately represented by the Ångström power law. However, the behaviour cannot be extended to the 1550 or 340–380 nm channels. In the UV spectral region, a decrease in the AOD slope is suspected. Unfortunately, the AOD errors in those channels do not let to come to any conclusions about this important point, which remains an open question for the second SAMUM campaign in Cape Verde in 2008.

The simulations performed with the OPAC model confirm the need of a water-soluble component in the desert aerosol to explain the observed variability of the AE, especially when the dust concentration was low. They also confirm the possibility of negative AE in desert dust, similar to those obtained in a short period in Ouarzazate. Finally, the comparison with the simultaneous measurements of several AERONET sites in the Saharan region confirm that a pure dust aerosol type was observed in Ouarzazate.

6. Acknowledgments

The authors thank the NOAA Air Resources Laboratory (ARL) for the provision of the HYSPLIT transport model and READY website (http://www.arl.noaa.gov/ready.html) used in this publication. We also acknowledge the AERONET PI's: P. Goloub and the LOA-PHOTONS team (Agoufou); A.M. Silva (Evora); S. Pugnaghi (Lampedusa); J. Cuesta (TamanrassetTMP); B. Mougenot of IRD; O. Hagolle of CNES and CESBIO (Ras El Ain) for their effort in establishing and maintaining the sites. The present study was supported by the German Research Foundation (DFG) within the Research Group SAMUM.

References

Arimoto, R. 2001. Eolian dust and climate: relationships to sources, tropospheric chemistry, transport and deposition. *Earth Sci. Rev.* **54**, 29–42.

Avila, A., Queralt-Mitjans, I. and Alarcón, M. 1997. Mineralogical composition of African dust delivered by red rains over north-eastern Spain. *J. Geophys. Res.* **102**, 21 977–21 996.

Ångström, A. 1961. Techniques of determining the turbidity of the atmosphere. *Tellus* **13**, 214–223.

Bergametti, G., Gomes, L., Coudé-Gaussen, G., Rognon, P. and Coustumer, M. 1989. African dust observed over Canary Islands: source regions identification and transport pattern for some summer situation. *J. Geophys. Res.* **94**, 14 855–14 864.

Chiapello, I., Moulin, C. and Prospero, J. M. 2005. Understanding the long-term variability of African dust transport across the Atlantic as recorded in both Barbados surface concentrations and large-scale Total Ozone Mapping Spectrometer (TOMS) optical thickness. *J. Geophys. Res.* **110**, D18S10.

D'Almeida, G. 1987. On the variability of desert aerosol radiative characteristics. *J. Geophys. Res.* **92**(D3), 3017–3026.

Draxler, R. and Rolph, G. 2003. HYSPLIT (HYbrid Single-Particle Lagrangian Integrated Trajectory) Model access via NOAA ARL READY Website (http://www.arl.noaa.gov/ready/hysplit4.html). Technical report, NOAA.

Dubovik, O., Holben, B., Eck, T., Smirnov, A., Kaufman, Y. and co-authors. 2002. Variability of absorption and optical properties of key aerosol types observed in worldwide locations. *J. Atmos. Sci.* **59**, 590–608.

Eck, T., Holben, B., Reid, J., Dubovik, O., Smirnov, A., O' and co-authors. 1999. The wavelength dependence of the optical depth of biomass burning, urban and desert dust aerosols. *J. Geophys. Res.* **104**, 31 333–31 350.

Freudenthaler, V., Esselborn, M., Wiegner, M., Heese, B., Tesche, M. and co-authors. 2008. Depolarization-ratio profiling at several wavelengths in pure Saharan dust during SAMUM 2006. *Tellus* **61B**, doi:10.1111/j.1600-0889.2008.00396.x.

Goudie, A. and Middleton, N. 2001. Saharan dust storms: nature and consequences. *Earth-Sci. Rev.* **56**, 179–204.

Guerzoni, S. and Chester, R. 1996. *The Impact of the Desert Dust Across the Mediterranean.* Kluwer Academic Publishers, Norwell, MA.

Gueymard, C. 1995. Smarts2, a simple model of the atmospheric radiative transfer of sunshine: algorithms and performance assessment. Report no. FSEC-PF-270-95, Florida Solar Energy Center. Cocoa, Florida.

Haywood, J., Francis, P., Dubovik, O., Glew, M. and Holben, B. 2003a. Comparison of aerosol size distributions, radiative properties, and optical depths determined by aircraft observations and Sun photometers during SAFARI 2000. *J. Geophys. Res.* **108** (D13), 8471, doi:10.1029/2002JD002250.

Haywood, J., Francis, P., Osborne, S., Glew, M., Loeb, N. and co-authors. 2003b. Radiative properties and direct radiative effect of saharan dust measured by the c-130 aircraft during shade, 1: solar spectrum. *J. Geophys. Res.* **108** (D18), 8577, doi:10.1029/2002JD002687.

Heintzenberg, J. 2008. The SAMUM-1 experiment over Southern Morocco: Overview and introduction. *Tellus* **61B**, doi:10.1111/j.1600-0889.2008.00403.x.

Hess, M., Koepke, P. and Schult, I. 1998. Optical Properties of Aerosols and Clouds: The Software Package OPAC. *Bull. Am. Meteorol. Soc.* **79**, 831–844.

Holben, B., Eck, T., Slutsker, I., Tanré, D., Buis, J. and co-authors. 1998. AERONET- a federated instrument network and data archive for aerosol characterization. *Remote Sens. Environ.* **66**, 1–16.

Holben, B., Tanre, D., Smirnov, A., Eck, T., Slutsker, I. and co-authors. 2001. An emerging ground-based aerosol climatology: aerosol optical depth from aeronet. *J. Geophys. Res.* **106**, 12 067–12 097.

Kandler, K., Deutscher, C., Ebert, M., Hofmann, H., Jäckel, S. and co-authors. 2008. Size distributions, mass concentrations, chemical and mineralogical composition, and derived optical parameters of the boundary layer aerosol at Tinfou, Morocco, during SAMUM 2006. *Tellus* **61B**, doi:10.1111/j.1600-0889.2008.00385.x.

Kasten, F. and Young, A. T. 1989. Revised optical air mass tables and approximation formula. *Appl. Opt.* **28**, 4735–4738.

Kaufman, Y. J., Tanré, D., Dubovik, O., Karnieli, A. and Remer, L. A. 2001. Absorption of sunlight by dust as inferred from satellite and groundbased remote sensing. *Geophys. Res. Lett.* **28**, 1479–1482.

Kaufman, Y. J., Koren, I., Remer, L. A., Tanré, D., Ginoux, P. and co-authors. 2005. Dust transport and deposition observed from the Terra-Moderate Resolution Imaging Spectroradiometer (MODIS) spacecraft over the Atlantic Ocean. *J. Geophys. Res.* **110**, D10S12.

Koepke, P., Hess, M., Schult, I. and Shettle, E. 1997. Global aerosol data set. Technical report, MPI Meteorologie Hamburg Report No. 243, 44 pp.

Mélice, J., Boughanmi, A., Eaton, F. and Wendler, G. 1984. Turbidity measurements of saharan aerosol and their effects on atmospheric heating and planetary reflectivity. *Arch. Met. Geoph. Biocl.* **B35**, 203–220.

Müller, T., Schladitz, A., Massling, A., Kaaden, N., Wiedensohler, A. and co-authors. 2008. Spectral absorption coefficients and refractive index of Saharan dust during SAMUM 2006. *Tellus* **61B**, doi:10.1111/j.1600-0889.2008.00399.x.

Myhre, G., Grini, A., Haywood, J., Stordal, F., Chatenet, B. and co-authors. 2003. Modeling the radiative impact of mineral dust during the Saharan Dust Experiment (SHADE) campaign. *J. Geophys. Res.* **108** (D18), 8579, doi:10.1029/2002JD002566.

Pace, G., di Sarra, A., Meloni, D., Piacentino, S. and Chamard, P. 2006. Aerosol optical properties at Lampedusa (Central Mediterranean), 1: influence of transport and identification of different aerosol types. *Atmos. Chem. Phys.* **6**, 697–713.

Petzold, A., Rasp, K., Weinzierl, B., Esselborn, M., Hamburger, T. and co-authors. 2008. Saharan dust absorption and refractive index from aircraft-based observations during SAMUM 2006. *Tellus* **61B**, doi:10.1111/j.1600-0889.2008.00383.x.

Prospero, J. 1999. Long range transport of mineral dust in the global atmosphere: impact of african dust on the environment of the south-eastern united states. *Proc. Natl. Acad. Sci. USA* **96**, 3396–3403.

Prospero, J. M., Ginoux, P., Torres, O., Nicholson, S. E. and Gill, T. E. 2002. Environmental characterization of global sources of atmospheric soil dust identified with the NIMBUS 7 Total Ozone Mapping Spectrometer (TOMS) absorbing aerosol product. *Rev. Geophys.* **40**(1), 1002, doi:10.1029/2000RG000095.

Raes, F., Bates, T., McGovern, F. and Liederkeke, M. 2000. The second aerosol characterization experiment (ACE2): general context and main results. *Tellus* **52B**, 111–126.

Rodríguez, S., Querol, X., Alastuey, A., Kallos, G. and Kakaliagou, O. 2001. Saharan dust contributions to PM10 and TSP levels in southern and eastern Spain. *Atmos. Environ.* **35**, 2433–2447.

Ryall, D., Derwent, R., Manning, A., Redington, A., Corden, J. and co-authors. 2002. The origin of high particulate concentrations over the United Kingdom, March 2000. *Atmos. Environ.* **36**, 1363–1378.

Seefeldner, M., Oppenreider, A., Rabus, D., Reuder, J., Schreier, M. and co-authors. 2004. A two-axis tracking system with datalogger. *J. Atmos. Ocean. Tech.* **21**, 975–979.

Smimov, A., Holben, B. N., Eck, T. F. and Dubovik, O. 2000. Cloud-Screening and Quality Control Algorithms for the AERONET Database. *Remote Sens. Environ.* **73**, 337–349.

Smirnov, A., Holben, B., Kaufman, Y., Dubovik, O., Eck, T. and co-authors. 2002. Optical properties of atmospheric aerosol in maritime environments. *J. Atm. Sci.* **59**, 501–523.

Sokolik, I. N., Winker, D. M., Bergametti, G., Gillette, D. A., Carmichael, G. and co-authors. 2001. Introduction to special section: outstanding problems in quantifying the radiative impacts of mineral dust. *J. Geophys. Res.* **106**, 18 015–18 027.

Stohl, A. 1998. Computation, accuracy and applications of trajectories: a review and bibliography. *Atmos. Environ.* **32**, 947–966.

Tanré, D., Devaux, C., Herman, M., Santer, R. and Gac, J. 1988. Radiative properties of desert aerosols by optical ground-based measurements at solar wavelengths. *J. Geophys. Res.* **93**, 14 223–14 231.

Tanré, D., Haywood, J., Pelon, J., Léon, J., Chatenet, B. and co-authors. 2003. Measurement and modeling of the Saharan dust radiative impact: overview of the Saharan Dust Experiment (SHADE). *J. Geophys. Res.* **108**, SAH 1.

Toledano, C., Cachorro, V., Berjon, A., de Frutos, A. M., Sorribas, M. and co-authors. 2007. Aerosol optical depth and Ångström exponent climatology at El Arenosillo AERONET site (Huelva, Spain). *Q. J. R. Meteorol. Soc.* **133**, 795–807.

von Hoyningen-Huene, W., Dinter, T., Kokhanovsky, A., Burrows, J. and M., D. 2008. Measurements of desert dust optical characteristic at Porte au Sahara during SAMUM. *Tellus* **61B**, doi:10.1111/j.1600-0889.2008.00405.x.

Wagner, F., Schreier, M., Seefeldner, M., Rabus, D. and Koepke, P. 2003. Ssara—a new and accurate sunradiometer—suitable for measuring dust. In: *Proceedings of the 2nd International Workshop on Mineral Dust*, 10–12 September, Paris, France.

Wagner, F., Bortoli, D., Pereira, S., Costa, M., Silva, A. and co-authors. 2008. Properties of dust aerosol particles transported to Portugal from the Sahara desert. *Tellus* **61B**, doi:10.1111/j.1600-0889.2008.00393.x.

Weinzierl, B., Petzold, A., Esselborn, M., Wirth, M., Rasp, K. and co-authors. 2008. Airborne measurements of dust layer properties, particle size distribution and mixing state of Saharan dust during SAMUM 2006. *Tellus* **61B**, doi:10.1111/j.1600-0889.2008.00392.x.

Werhli, C. 2000. Calibration of filter radiometers for determination of atmospheric optical depth. *Metrologia* **37**, 419–422.

Wiegner, M., Gasteiger, J., Kandler, K., Weinzierl, B., Rasp, K. and co-authors. 2008. Numerical simulations of optical properties of Saharan dust aerosols with emphasis on linear depolarization ratio. *Tellus* **61B**, doi:10.1111/j.1600-0889.2008.00381.x.